Article

Modi-Red Mud Loaded CoCatalyst Activated Persulfate Degradation of Ofloxacin

Qu Wu, Wenquan Sun, Kinjal J. Shah [ID] and Yongjun Sun *[ID]

College of Urban Construction, Nanjing Tech University, Nanjing 211800, China
* Correspondence: sunyongjun@njtech.edu.cn

Abstract: As an abundant potentially dangerous waste, red mud (RM) requires a straightforward method of resource management. In this paper, an RM catalyst loaded with cobalt (Co-RM) was prepared by the coprecipitation method for the efficient activation of persulfate (PS). Its degradation performance and mechanism of ofloxacin (OFL) were investigated. The characterization results of scanning electron microscopy, X-ray diffractometer, and energy dispersive spectrometer showed cobalt was successfully loaded onto the surface of RM, and the catalyst produced could effectively activate PS. Under the conditions of 15 mg/L OFL, 0.4 g/L Co-RM, 4 g/L PDS, 3.0 pH, and 40 °C temperature, the maximum removal rate of OFL by the Co-RM/PDS system was 80.06%. Free radical scavenging experiments confirmed sulfate radicals were the main active substances in the reaction system. The intermediates in OFL degradation were further identified by gas chromatography-mass spectrometry, and a possible degradation pathway was proposed. Finally, the relationship between defluorination rate and time in the Co-RM/PDS degradation OFL system was described by the first-order kinetic equation. This work reports an economical, environmental solution to the use of waste RM and provides a research basis for the further exploration of RM-based catalysts.

Keywords: red mud; persulfate; ofloxacin; degradation pathway; defluorination

1. Introduction

In recent years, the spatial distribution of pharmaceuticals and personal care products (PPCPs) occurs widely in the aquatic environments of industrialized and developing countries. PPCPs are acknowledged as emerging contaminants in water resources and one of the most dangerous ingredients of pharmaceuticals used in human and animal medicines [1]. Among various PPCPs, residues of antibiotics in water have attracted much attention due to their ecological risks [2,3]. Ofloxacin (OFL) is a bactericidal antibiotic that can inhibit the synthesis and replication of bacterial DNA, thereby achieving rapid sterilization [4]. With the wide use of OFL, its abuse is more serious. Compared with other antibiotics, OFL exhibits a high degree of excretion of unmetabolized molecules into the environment via wastewater treatment plants [5]. OFL also has an antibacterial action on beneficial microorganisms that assist wastewater treatment, so it is difficult to biodegrade. Furthermore, the complex composition, large water volume, and large distribution of OFL render eliminating it from wastewater through conventional treatment processes, such as biological methods, is challenging. In addition, due to the concept of clean production and zero emission of environmental protection requirements, making this kind of waste water environmental policy becomes difficult [6].

Currently, the main methods for treating OFL effluents include physicochemical processes, biological treatment, and advanced oxidation processes [7,8]. The physicochemical process is usually used as a pretreatment technology for refractory sewage, and the purpose of deep purification is achieved through repeated use [9]. The most common physicochemical methods are adsorption [10] and membrane separation [11]. Adsorption accumulates pollutants from the water in the adsorbent to generate new solid waste [12]. Membrane

separation technology has the disadvantages of easy fouling of the filter membrane, low stability, and limited scope [13]. The biological process is a widely used antibiotic wastewater treatment that breaks down antibiotics in wastewater through microbial metabolism. However, when the type or concentration of antibiotics in the wastewater changes substantially, redomesticating and culturing microorganisms become necessary. Failure to respond in a timely manner can affect microbial metabolism and lead to the breakdown of microbial systems. Compared with other physical and biological treatment technologies, advanced oxidation has a good refractory removal effect [14]. It neither transfers pollutants from one stage to another (e.g., chemical precipitation and adsorption) nor produces large amounts of hazardous sludge [15]. In recent years, the advanced oxidation technology based on $SO_4^-\cdot$ has attracted a large amount of attention in the treatment of antibiotic loads due to its high oxidation potential. Compared with $\cdot OH$, $SO_4^-\cdot$ has the advantages of higher redox potential, broader pH range, and longer half-life [16,17].

The advanced oxidation technology based on sulfate radicals ($SO_4^-\cdot$) is widely used in the field of antibiotic wastewater treatment. The production of sulfate radical is mainly based on the activation of persulphate. However, persulfate (PS) must be activated in use to have strong oxidation. UV, heat, microwave, electrochemistry, and transition metals can activate PS [18–21]. However, UV and heat activation requires excessive energy consumption and high cost [13]. Electrochemical activation of PS has drawbacks such as low current efficiency and limitation of mass transfer [22]. Transition-metal-promoted PS has the advantages of low energy consumption, remarkable effect, and great potential for catalyst recycling [23]. The usual catalysts for transition metal ions are iron, cobalt, and copper [24]. Among them, the transition metal cobalt ion (Co^{2+}) has a good catalytic effect and can effectively activate PDS to produce active species such as $SO_4^-\cdot$ [25]. However, in a homogenous Co-PDS system, the dosage of cobalt ions in the application is extremely high, much more than the emission standard, restricting its wide application [26]. Therefore, cobalt-based heterogeneous catalysts need to be investigated to improve efficiency, reduce the dissolution of cobalt ions, and reduce their damage to the environment.

Red mud (RM) is a solid waste resulting from alumina smelting. It contains a large amount of transition metals and has a strong alkalinity that is potentially harmful to the natural environment [27]. RM contains Al_2O_3, Fe_2O_3, and TiO_2 [28]. It has a large surface area and can be used for waste water and exhaust gas purification [29]. It is economical and practical with rich metal components and fine grain distribution. The coexistence of multiple metals can stimulate synergistic catalysis between transition metals. The use of RM as an environmental remediation material is a new hotspot in the current research field. It has many advantages such as a simple procedure and low cost in the application [30]. Research on the application of RM in the field of environmental protection should be strengthened, and the large-scale application of RM in the field of environmental rehabilitation with more mature technology should be promoted. Peroxides have been successfully activated using RM loaded with transition metals. However, research into the activation of PS by RM is insufficient, and its application on emerging organic pollutants remediation has not been well explored.

In this paper, the fluoroquinolone antibiotic OFL was used as the target pollutant to explore the degradation efficiency and reaction mechanism of OFL in the Co-RM/PDS system. Different characterization methods were applied to analyze the physical and chemical properties of Co-RM. The effects of PDS dosage, Co-RM dosage, reaction temperature, pH, and initial concentrations on the removal rate of OFL were investigated. The main active species in the reaction system were determined by radical quenching experiments. Headspace chromatography mass spectrometer (GC-MS) was used to identify the degradation pathway of OFL. Finally, the removal effect of Co-RM-activated PDS on F^- in OFL was examined by the fluoride ion selective electrode. This work aims to provide a theoretical reference for the extensive use of RM and the removal of emerging fluoroquinolone antibiotic contamination.

2. Materials and Methods

2.1. Experimental Materials

RM was created in the production of alumina by Bayer process provided by a company in Chongqing (China). Due to the strong alkalinity of the original RM, it was pretreated by acid modification in advance. The main chemical components are shown in Table 1. OFL ($C_{18}H_{20}FN_3O_4$, 98%) and sodium persulfate ($Na_2S_2O_8$, 99%) were purchased from Shanghai McLean Biochemical Technology Co., Ltd. (Shanghai, China) Cobalt nitrate hexahydrate ($Co(NO_3)_2 \cdot 6H_2O$, 99%), hydrochloric acid (HCl), tert-butanol (TBA), ethanol (EtOH), and sodium hydroxide (NaOH) were purchased from Nanjing Chemical Reagent Co., Ltd. (Nanjing, China). Sodium thiosulfate ($Na_2S_2O_3 \cdot 5H_2O$) was purchased from Shanghai Lingfeng Chemical Reagent Co., Ltd. (Shanghai, China). The above experimental drugs were analytically pure. Laboratory water was deionized water.

Table 1. Main chemical composition of RM.

Composition	CaO	Al_2O_3	SiO_2	Na_2O	TiO_2	Fe_2O_3
Content (wt%)	4.12	30.13	34.55	14.51	4.46	12.23

2.2. Preparation and Characterization of Co-RM Catalyst

Figure 1 shows the flow chart of the preparation of Co-RM. The RM was dried in an oven to remove moisture, ground through an 80-mesh standard sieve, added to a hydrochloric acid solution with a concentration of 4 mol/L, stirred at room temperature for several hours, and dried at 80 °C for 8 h to obtain acidified modified RM. Then, 5 g of acidification pretreatment RM was weighed, dried by natural ventilation, and ground through a 150-mesh sieve. The 0.1 M cobalt nitrate hexahydrate and 0.5 M sodium carbonate solution were added dropwise to the beaker pre-loaded with RM, and continuously stirred at a constant speed in a constant temperature water bath at 60 °C. After the precipitation was completed, the suspension was continuously stirred at 60 °C. After aging for 1 h, suction filtration separation was performed. The modified RM after suction filtration was dried at 100 °C, transferred to a muffle furnace, and calcined at 400 °C for 4 h to prepare a modified RM catalyst (Co-RM).
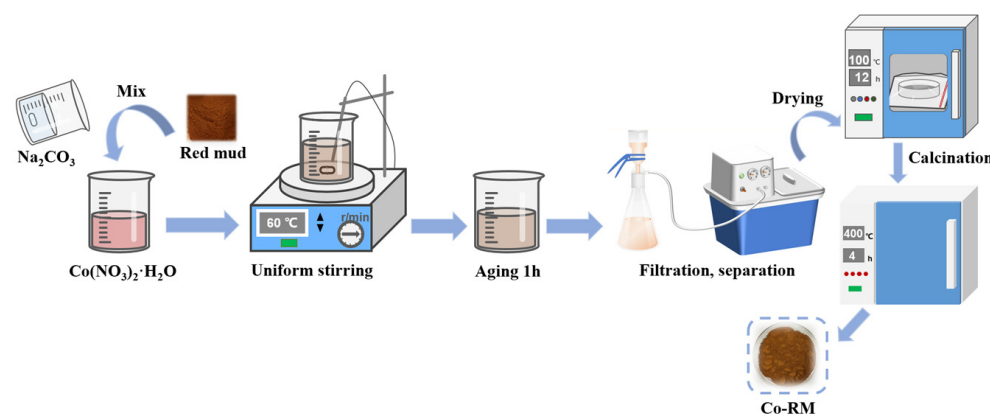

Figure 1. Flow chart of preparation of Co-RM.

The surface of Co-RM catalyst was analyzed by scanning electron microscopy (SEM, S-3400N, Hitachi, Tokyo, Japan). The material structure and crystal structure of the catalyst were detected by X-ray diffractometer (XRD, X 'TRA, Thermo Fisher Scientific, Waltham, MA, USA). The XRD pattern was used to determine whether the metal ion loading affected the structure of the RM catalyst. The elemental composition of the samples was analyzed by an X-ray energy dispersive spectrometer (EDS). The pore size and surface area of the modified RM catalyst were determined by pore size and specific surface area analysis

(BET, Novawin 1994–2016, Quantachrome, Boynton Beach, FL, USA). Zeta potential (ZP) measurement of obtained microparticles was carried out on Zetasizer Nano ZS90 (Malvern Instruments Ltd., Malvern, UK).

2.3. OFL Degradation Experiment

The OFL degradation experiment was performed on a magnetically heated stirrer. First, 200 mL of OFL solution with a mass concentration of 15 mg/L was placed in a beaker. A certain amount of PDS or RM has been added. The reaction was carried out at a certain temperature and in the dark (pH was not adjusted). Then, 5 mL of samples were taken every 10 min, immediately quenched with 30 μL $Na_2S_2O_3$ solution with a substance concentration of 0.1 mol/L and passed through a 0.45 μm filter membrane. The OFL concentration was analyzed with a UV-Vis spectrophotometer (UV-Vis, UV-5500PC, Shanghai Yuan Analysis Instrument Co., Ltd., Shanghai, China) at the wavelength of 294 nm, as shown in Figure S1 [31].

2.4. Degradation Product Analysis

Free radical scavenging experiments were used to investigate which active groups ($SO_4^-\cdot$ and HO·) play a major role in the PS oxidation reaction. Various quenchers were added to the reaction system. Ethanol (EtOH) can react rapidly with sulfate radicals and hydroxyl radicals at the same time, whereas tert-butyl alcohol (TBA) can react rapidly only with HO·. Thus, when EtOH alone is added to the reaction system, $SO_4^-\cdot$ and HO· can be trapped at the same time. When TBA alone is added, HO· can be quenched in the system. Comparing the degradation of OFL in the two reaction systems can identify which active group plays a major role in the reaction.

To examine the degradation pathway of OFL after oxidation, the sample solution was filtered through a 0.45 μm membrane after the reaction and added to the liquid vial via a syringe. Any intermediate product occurring during the reaction was analyzed by GC-MS (Thermo Trace 1310, Thermo Fisher Scientific, USA). A fluoride ion selective electrode (PXSJ-216F, Shanghai Yizheng Scientific Instrument Co., Ltd., Shanghai, China) was used to measure the mass concentration of fluoride ions in the solution before and after the reaction, and the rate of defluorination of OFL in the Co-RM/PDS system was further examined.

3. Results and Discussion

3.1. Catalyst Characterization

The RM samples were cleaned and dried to constant weight at 60 °C for pore size and specific surface area tests. The N_2 adsorption–desorption isotherms of the pristine RM and Co-RM catalyst are shown in Figures S2 and S3. According to the relevant International Union of Pure and Applied Chemistry (IUPAC) standards, the two isotherms in the figure belong to Type II [32,33]. In addition, an H3-type hysteresis band was observed in both samples [34]. The generated hysteresis loop is small, indicating that there is a small amount of mesopores [35]. The pore size distribution of Co-RM is narrow, indicating that the pore structure of Co-RM is mainly micropores and a small amount of mesopores. At a relative pressure of about 1, the N_2 absorption increases further, indicating the sample contains large pores [36]. Figures S2 and S3 shows the adsorption amount of N_2 by Co-RM is larger than that by RM. Depending on the adsorption of N_2 on the catalyst surface, the specific surface area of different RM catalysts can vary and can be calculated using the BET adsorption isotherm model (Table 2). The specific surface area of the two RM catalysts is RM < Co-RM, and the larger specific surface area plays a positive role in the subsequent catalysis.

Figure S3b shows Co-RM contains more micropores than RM, which is the main reason for the high specific surface area of Co-RM. The pore distribution of Co-RM has evident peaks, and the peaks of the most probable pore size [37] (the pore size with the highest probability of pore occurrence) are 17.91, 45.38, and 119.36 nm, which indicates Co-RM has not only micropores but also mesopores with large pore volume [38]. It peaked at 17.91 nm,

indicating the addition of Co increases the pore structure and changes the surface structure of the catalyst. Therefore, compared with RM, Co-RM has a larger specific surface area and a developed pore structure.

Table 2. Textural properties of RM and Co-RM determined by N2 adsorption–desorption isotherms.

Sample	BET Surface Aera (m^2/g)	Pore Volume (cm^3/g)	Average Pore Diameter [a] (nm)	Average Pore Diameter [b] (nm)
RM	215.65	0.41	9.07	8.64
Co-RM	431.22	0.75	12.65	11.77

Average pore diameter [a]: BJH adsorption average pore diameter; Average pore diameter [b]: BJH desorption average pore diameter.

The SEM images of RM and modified Co-RM samples are shown in Figure 2a–d. Figure 2a shows RM consists mainly of rhombohedral particles [39]. The particles are aggregated in a disorderly manner, the surface is rough and porous, and the pore distribution is uneven. Figure 2a,c shows the original RM and the modified loaded RM have slit-like pores, which is also consistent with the H3-type hysteresis loop observed in the N$_2$ adsorption–desorption isotherm. Comparing Figure 2a,b and Figure 2c,d reveals Co metal loading and calcination treatment influence the morphology of RM. The surface of the modified RM forms an irregular pore structure, and the pores enlarge. The specific surface area of the RM increases, which can further increase the number of active sites of the RM catalyst and improve the catalytic effect.
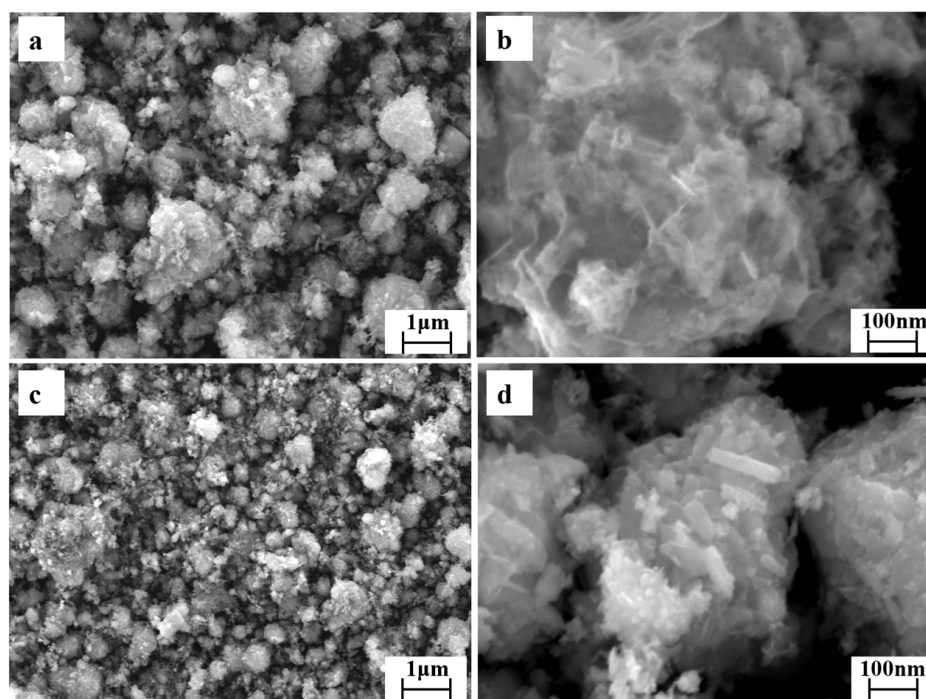

Figure 2. SEM image of the original (**a**,**b**) and loaded RM (**c**,**d**).

Figure S4 is the EDS spectrum of modified RM. The analysis results show the basic elements of RM include O, Al, Fe, Na, and C, with O and C occupying a larger proportion. In this paper, the RM catalyst loaded with transition metal cobalt was prepared by coprecipitation methods. Figure S4 shows the transition metal cobalt was successfully loaded onto the surface of RM and distributed evenly, proving the modified catalyst designed in this experiment was fabricated effectively.

To investigate the crystal structure of the original RM and the Co-modified RM samples, the XRD test of the catalyst samples used in the experiment was performed. The experimental results are shown in Figure 3. The main substances in the RM samples are hematite, quartz, and boehmite. The most characteristic peaks of the three samples are Fe_2O_3 (JCPDS #86-055) appearing at 33.1 and 35.6. Calcination and metal loading do not remarkably affect the crystal structure of RM. The diffraction peaks in RM and Co-RM are the same. In addition to the widespread Fe_2O_3, the sample contains SiO_2, $AlO(OH)$, $NaAlSi_3O_8$, and $FeO(OH)$, which also agrees with the results of the EDS analysis. The supported cobalt RM catalyst prepared in this paper did not appear as the material crystal phase of cobalt in the XRD pattern, but the cobalt element was detected in the energy spectrum analysis. The reason might be that the intensity of the diffraction peak of CoO or Co_3O_4 was low and the peak was very broad, which cannot be clearly observed in the XRD pattern. This result indicated that the crystallinity of cobalt on the RM surface was relatively low and had a small average particle size. The small particle size could ensure the loaded metal maintained a good dispersion state in the catalytic reaction and improved the catalytic activity and stability.
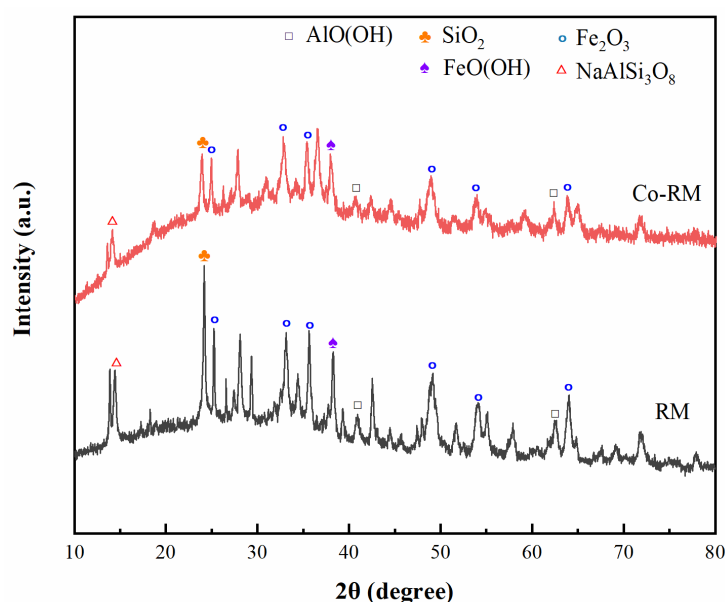

Figure 3. XRD patterns of RM and Co-RM.

3.2. Removal Rate of OFL in Different Reaction Systems

The removal rate of OFL under different reaction systems was investigated under the conditions of OFL mass concentration of 15 mg/L, PDS dosage of 4 g/L, catalyst dosage of 0.4 g/L, reaction system pH = 3.0, and temperature of 40 °C.
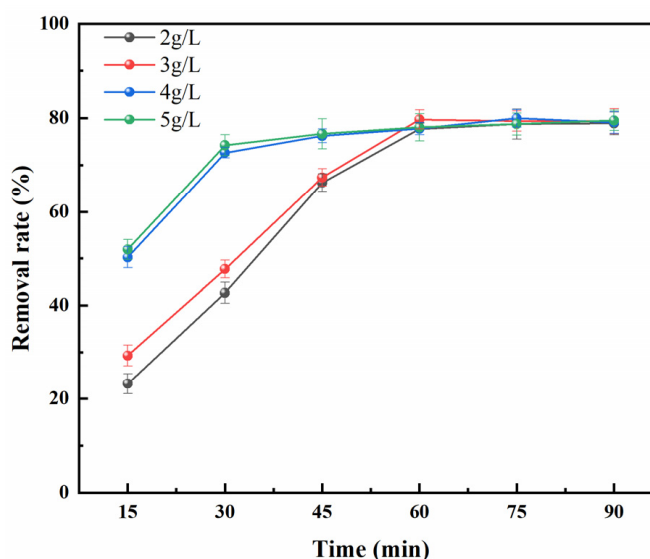
Figure S2 shows Co-RM degraded only 19.48% of OFL in 90 min. The removal rate of OFL was 29.48% after 90 min of reaction in the presence of PDS alone. A possible explanation is that PDS produced active species after thermal excitation, which caused oxidative degradation of partial OFL. Compared with the RM + PDS/OFL system, after adding Co-RM and PDS to the solution, the removal rate of OFL was 80% after 90 min, and the removal rate considerably improved. This result indicated Co-RM effectively activated PDS to produce active species with strong oxidizing properties, and Co was the active component of the catalyst.

3.3. Analysis of Influencing Factors of OFL Degradation Experiment

3.3.1. Effect of PDS Dosage on OFL Removal Rate

Figure 4 shows when the PS injection amount was in the range of 2 g/L to 5 g/L, the removal rate of OFL in the reaction system was positively correlated with the amount of

PS. The removal rates of OFL in the Co-RM/PDS system after 90 min of reaction were 78%, 79.01%, 80%, and 79.51% when the PS injection amounts were 2, 3, 4, and 5 g/L, respectively. With increasing reaction time, the OFL removal rate showed a trend of rapidly increasing, then slowly increasing, and finally remaining stable. When the PDS dosage was increased from 2 g/L to 3 g/L, the OFL removal rate increased less sharply from 41.5% to 48%. After 60 min of reaction, the maximum OFL removal rate was 80%. As the PDS dosage further increased from 3 g/L to 5 g/L, the OFL removal rate increased substantially from 48% to 76%, and the OFL removal rate gradually peaked after 30 min of the reaction with a maximum removal rate of 76%.
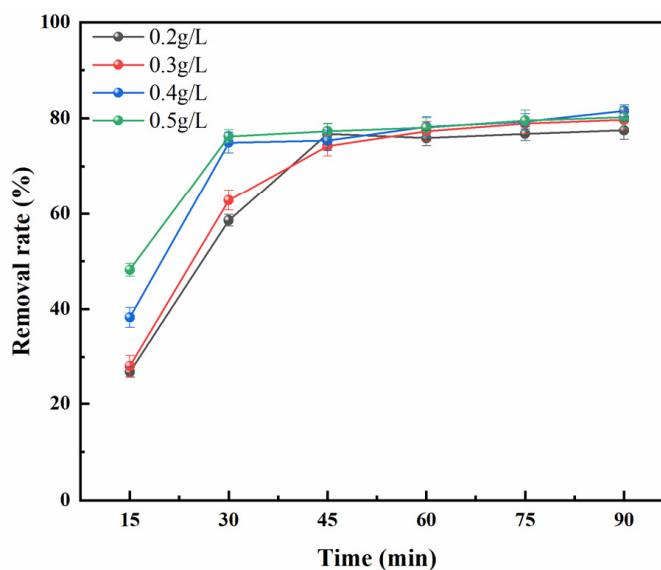

(Experimental condition: $[OFL]_0$ = 15 mg/L, $[Co\text{-}RM]_0$ = 0.4 g/L, and T = 40 °C)

Figure 4. Effect of PDS dosage on OFL removal rate.

Figure 4 shows that in the Co-RM/PDS system, the removal rate of OFL increases with the increase in PDS dosage. When the PDS dosage increased from 3 g/L to 4 g/L, the removal rate of OFL increased greatly mainly because PS is the only source of sulfate radicals in water. The higher the dosage is, the more sulfate radicals are produced. Increasing the mass concentration of PDS can provide more reaction sites. When the dosages of PDS were 4 and 5 g/L, the removal rate of OFL reached 80% and 79.74% at 75 min, respectively, and changed slightly after 15 min. The increase in PDS dosage had a minimal effect on the removal rate of OFL, which may be due to the self-quenching reaction between excessive free radicals [40]. As a result, the removal rate of OFL in the reaction system was inhibited. Alternatively, the active substances HO· and SO_4^-· produced were further converted into less active SO_5^-· and HSO_4 [41,42].

3.3.2. Effect of Co-RM Dosage on OFL Removal Rate

Figure 5 shows that at Co-RM catalyst dosages of 0.2, 0.3, 0.4, and 0.5 g/L, the removal rates of OFL in the Co-RM/PDS reaction system were 77.49%, 79.68%, 81.56%, and 80.23% after 90 min, respectively. Figure 5 shows that with increasing catalyst dosage, the removal of OFL first increases and then decreases. The removal rate of OFL increased rapidly with increasing reaction time within 30 min prior to reaction. After 30 min of reaction, the removal rate of OFL slowly increased with increasing reaction time. With a Co-RM dosage of 0.4 g/L and a reaction time of 90 min, the removal rate of OFL was highest, and the maximum removal rate was 81.56%.

(Experimental condition: $[OFL]_0 = 15$ mg/L, $[PDS]_0 = 4.0$ g/L, and T = 40 °C)
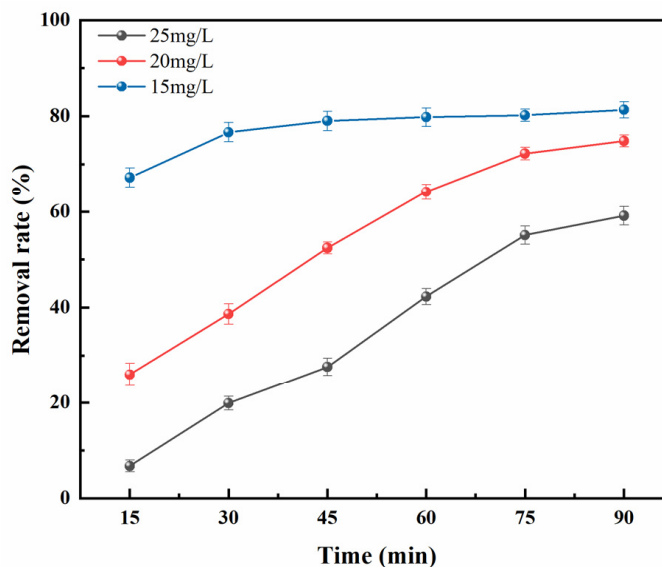
Figure 5. Effect of Co-RM dosage on OFL removal rate.

Figure 5 shows that with increasing Co-RM dosage, the removal rate of OFL in the Co-RM/PDS system first increases and then gradually decreases. Within 30 min after the reaction, the OFL removal rate increased with increasing catalyst dosage because increasing Co-RM dosage provided more active sites for the reaction. At a catalyst dosage of 0.4 g/L, the OFL removal rate was 81.56%. As the catalyst dosage increased further to 0.5 g/L, the removal rate decreased. This phenomenon may be due to the decomposition reaction between excess free radicals generated by an excess catalyst, and the decrease in free radicals led to a decrease in OFL removal rate [43]. No remarkable change in degradation efficiency was observed after adding excess catalyst, which may be because the concentration of PS cannot meet requirements. As the dosage of the Co-RM catalyst further increases in the reaction system, the OFL removal rate is only slightly improved because when the amount of the catalyst in the reaction system is small, the catalytic sites provided by the catalyst are limited and the number of free radicals generated is limited. To save costs, the dosing of catalyst and oxidant in the reaction system needs to be controlled. The goal is to reduce the most pollutants at the lowest cost. Therefore, the optimal dosage of Co-RM in the Co-RM/PDS reaction system in this experiment is 0.4 g/L.

3.3.3. Effect of Initial OFL Concentration on OFL Removal Rate

Under the conditions of 40 °C, Co-RM catalyst dosage of 0.4 g/L, and PDS dosage of 4 g/L, the initial concentration of OFL was controlled to 10–20 mg/L to show the effect of various initial concentrations of OFL during catalytic degradation. The results are shown in Figure 6. In the Co-RM/PDS reaction system, the removal rate of OFL gradually decreased as the concentration increased. When the initial concentration of OFL was 10 mg/L, the removal rate of OFL after 90 min was 81.32%. When the initial concentration of OFL increased to 15 mg/L, the removal rate of OFL decreased to 74.84% after 90 min. When the Initial concentration of OFL was further increased to 20 mg/L, the OFL removal rate decreased to 59.12%. This result shows the removal rate of OFL is inversely proportional to the initial concentration of OFL, and the removal effect is better in low-concentration OFL wastewater. This result has two main reasons: (1) Under the same dosage of catalyst and oxidant, the number of free radicals generated by activation of the Co-RM/PDS system is approximately the same. When the pollutant concentration is lower, the greater the number of oxidative free radicals, the larger the likelihood of oxidation. Therefore, the system with lower pollutant concentration has a higher removal rate of pollutants. (2) When the initial concentration of the pollutant is very low, fewer intermediate products are produced in the

oxidation, making OFL dominant in the competitive reaction and easier to be oxidized. In summary, in the Co-RM/PDS reaction system, the smaller the initial concentration of OFL is, the higher the OFL removal rate.
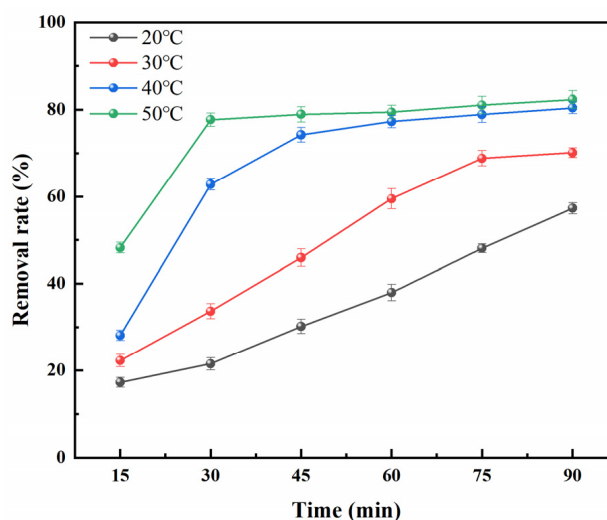

(Experimental condition: $[Co\text{-}RM]_0 = 0.4$ g/L, $[PDS]_0 = 4.0$ g/L, and T = 40 °C)

Figure 6. Effect of initial concentration on OFL removal rate.

3.3.4. Effect of Temperature on OFL Removal Rate

Under the conditions of a Co-RM catalyst dosage of 0.4 g/L, a PDS dosage of 4 g/L, and an initial OFL mass concentration of 15 mg/L, the temperature of the reaction system was controlled at 20–50 °C, and the effects of different temperature conditions on the removal rate of OFL in the reaction system were studied. The results are shown in Figure 7. The removal rate of OFL increases with increasing temperature. With a reaction time of 90 min and a reaction temperature of 20 °C, the OFL removal rate was 57.27%. At a reaction temperature of 30 °C, the removal rate of OFL was 70.13%. When the reaction temperature was increased to 40 °C and 50 °C, the removal rates of OFL in the reaction system increased to 80.41% and 82.33%, respectively.
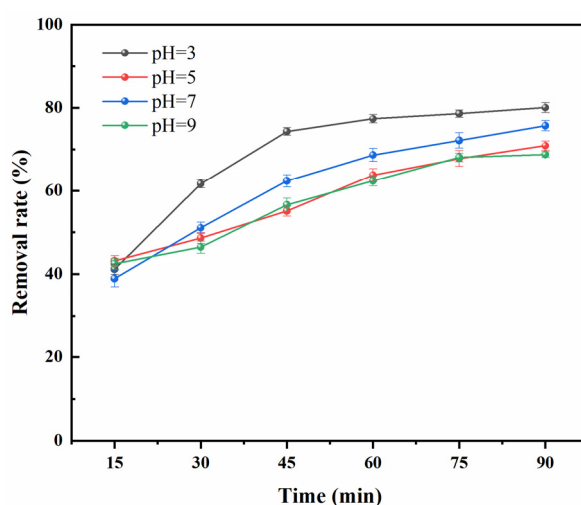

(Experimental condition: $[Co\text{-}RM]_0 = 0.4$ g/L, $[PDS]_0 = 4.0$ g/L, and $[OFL]_0 = 15$ mg/L)

Figure 7. Effect of temperature on OFL removal rate.

The results of Figure 7 show that under appropriate temperature conditions, increasing the reaction temperature can accelerate the reaction rate of the Co-RM/PDS system, expedite the formation of free radicals and non-radical active species, and promote OFL degradation because thermal activation is one of the ways to activate PS. Increasing the temperature can not only break the dioxygen bond in the PS but also generate sulfate radicals. At the same time, increasing the temperature can promote the collision frequency between the molecules on the catalyst surface [44]. Therefore, PS in the reaction system can be activated in two ways, so sulfate radicals can be produced in large quantities. According to Le-Chatelier principle, the increase in temperature can promote the positive course of the endothermic reaction, which means the reaction can move from the equilibrium state to the positive reaction direction [45]. In the Co-RM/PDS reaction system, Co-RM activates PS as an endothermic reaction, so increasing the temperature can generate a large amount of sulfate radicals, thereby improving the oxidation capacity of the system.

3.3.5. Effect of pH on OFL Removal Rate

OFL exists in an aqueous solution in different concentrations under dissimilar pH conditions. Under the conditions of 40 °C, a Co-RM catalyst dosage of 0.4 g/L, a PDS dosage of 4 g/L, and an initial OFL bulk concentration of 15 mg/L, the initial pH of the solution set to 3–9. The effect of the Co-RM/PDS system on OFL removal when the initial pH values were 3.5 and 7.9 were investigated. The results are shown in Figure 8. The removal rate of OFL gradually decreased from 77.28% to 63.75% after 45 min of reaction with the increase of pH in the range of 3–7. After 90 min of reaction at pH = 3, the removal rate of OFL was 81.06% and reached the maximum. At pH = 9, the OFL removal rate was 68.73% after 90 min under alkaline conditions.

(Experimental condition: $[Co\text{-}RM]_0 = 0.4$ g/L, $[PDS]_0 = 4.0$ g/L, $[OFL]_0 = 15$ mg/L, and T = 40 °C)

Figure 8. Effect of pH on OFL removal rate.

In the pH range examined, OFL is present in the form of cations. At pH = 3, $H_2SO_8^{2-}$ is the main form of PDS. As shown in Figure S5, the surface of Co-RM is positively charged and the ability to adsorb PDS is enhanced [46]. The reaction creates a more active substance $SO_4^-\cdot$, which quickens the interaction with OFL and promotes OFL degradation. With the increase in solution pH, the surface charge and PDS morphology are affected by Co-RM, which affects the interaction between the catalyst and PDS, which is not conducive to the activation of PDS and the formation of free radicals, resulting in the decrease of OFL removal rate. When the solution is in a super alkaline state, the oxidizing ability of the reaction system is inhibited because, in different pH environments, the types and amounts of free radicals generated by PDS activation are very diverse. If the pH of the solution is greater than 7, three reactions are possible. The first is the self-extinguishing effect

of $SO_4^-\cdot$. Second, a large amount of OH^- in the solution can react with $SO_4^-\cdot$ to form $HO\cdot$. The third is the reaction between $SO_4^-\cdot$ and $S_2O_8^{2-}$ [47]. In these three reactions, the self-extinguishing effect of $SO_4^-\cdot$ dominates, so the total amount of active species in the reaction system decreases continuously, and the rate of degradation of pollutants gradually decreases.

3.4. Analysis of OFL Degradation Pathway

In the reaction, in addition to the activation of PS by the Co-RM catalyst to generate sulfate radicals, hydroxyl radicals are generated because, in the reaction, $SO_4^-\cdot$ can also react with H_2O to form $HO\cdot$. Therefore, when the activated PDS process is used to degrade the target pollutants, the reaction system generally has two active species, namely $SO_4^-\cdot$ and $HO\cdot$. To clarify which active group plays a major role in the degradation reaction, the radical scavenger experiments were carried out with anhydrous ethanol (ETOH) and tert-butanol (TBA) as quenchers [8,48]. Among them, EtOH can quench $SO_4^-\cdot$ and $HO\cdot$, and TBA can be used as an $HO\cdot$ quencher because TBA reacts with $HO\cdot$ faster than $SO_4^-\cdot$. Figure 9 shows TBA and EtOH have some inhibitory effect on the removal rate of OFL in the Co-RM/PDS reaction system, and the inhibition of OFL degradation in the reaction system increases with increasing concentration of quencher TBA and EtOH. With the addition of TBA, the removal rate of OFL in the reaction system decreased by 24.70%. In the case of adding EtOH alone, the removal rate of OFL decreased by 36.83% after 90 min.
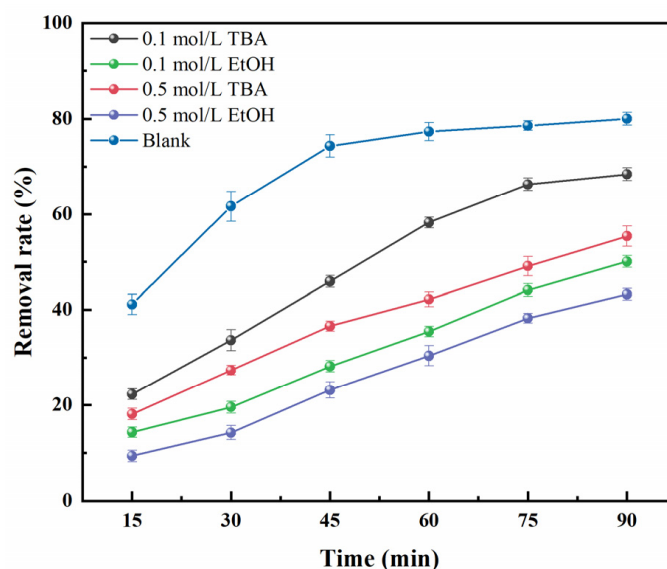

Figure 9. Free radical trapping experiment of Co-RM/PDS system.

Figure 9 shows the removal rate of OFL was slightly inhibited after adding different concentrations of TBA into the Co-RM/PDS system. However, when different concentrations of EtOH were added to the reaction system, the inhibition of RM-activated PS degradation of OFL was very evident. When the concentration of EtOH was 0.1 mol/L, the removal rate of OFL was 50.08% after 90 min of reaction. When 0.5 mol/L EtOH was added to the reaction system, the removal rate of OFL was further reduced. This outcome suggests $SO_4^-\cdot$ and $HO\cdot$ are involved in the degradation of OFL, but compared with $HO\cdot$, $SO_4^-\cdot$ contributes more substantially to the degradation of OFL by Co-RM-activated PDS, indicating $SO_4^-\cdot$ plays an important role, and $HO\cdot$ plays a supporting role. Hence, the active main group in the Co-RM/PDS reaction system is $SO_4^-\cdot$.

To elucidate the degradation pathway of OFL in the Co-RM/PDS system, the intermediate products formed during the degradation were determined using GC-MS. The OFL degradation products identified via GC-MS are summarized in Table S1. Moreover, the evolution of corresponding products was proposed, which was involved in three predomi-

nant pathways and illustrated in Figure 10. The potential degradation pathways of OFL at Co-RM/PDS system include piperazine, defluorination, demethylation, decarboxylation, hydroxylation, and ring opening [49–51]. The molecules gradually became smaller as the reaction time increased, indicating OFL was effectively decomposed, and 11 intermediates (P1–P11) had protonated molecules and ions at m/z of 318, 290, 149, 274, 212, 145, 363,12, 321, 278, 388, and 386. In pathway (1), P1($C_{17}H_{20}FN_3O_2$) was formed by decarboxylation of OFL, and then F^- was replaced by SO_4^-· to obtain P2 ($C_{15}H_{19}N_3O_2$) [52]. Finally, P3($C_{10}H_{15}N$) was formed by ring opening and defluorination. The products P4 ($C_{15}H_{16}N_3O_2$), P5 ($C_{11}H_9NO_2$) [53,54], and P6 (C_9H_7NO) were non-selective SO_4^-· and HO· attacking the piperazine group in OFL, which were obtained by P1 defluorination, piperazine bond cleavage, and ring opening. In pathway (2), first, the methyl group on the OFL molecule was replaced by the hydroxyl group, resulting in the conversion of the OFL molecule into P7 ($C_{17}H_{18}FN_3O_5$) [55]. Subsequently, after the dehydroxylation reaction, P7 was further attacked by active species to generate the intermediates P8 ($C_{15}H_{16}FN_3O_4$) and P9 ($C_{13}H_{11}FN_2O_4$) [56]. Reaction pathway (3) was to carboxylate OFL to obtain P10 ($C_{18}H_{16}FN_3O_6$) and P11 ($C_{18}H_{14}FN_3O_6$) by HO· attack [57]. Finally, through a series of complex degradation reactions, these intermediates can be further oxidized to smaller molecular compounds and mineralized to CO_2, H_2O, F^-, and NH_4^+ [58].
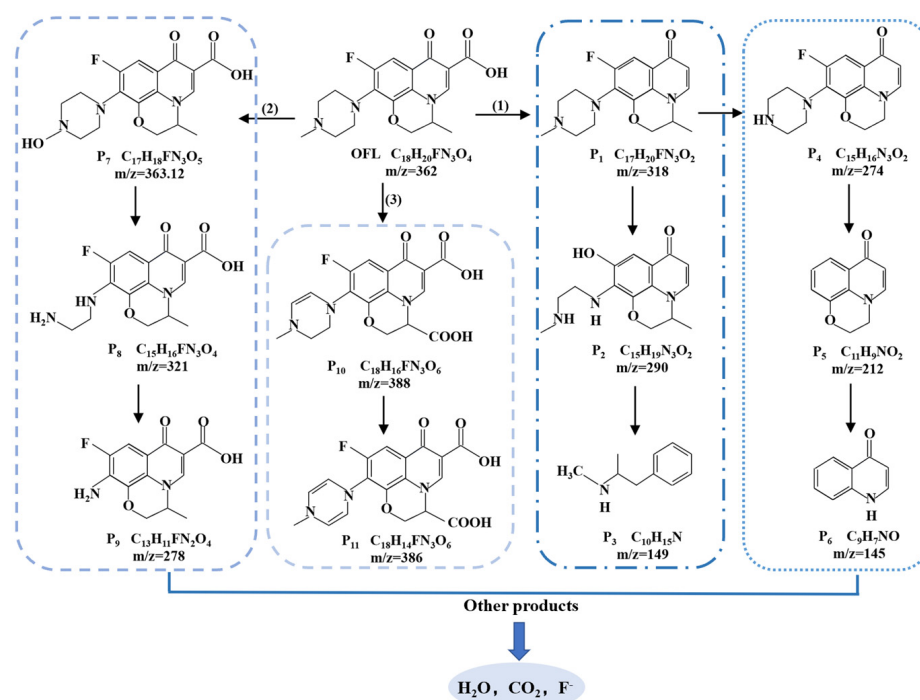

Figure 10. Possible degradation pathways of OFL by Co-RM/PDS system.

3.5. Analysis of Co-RM Activated PDS Defluorination Effect

To investigate further the transformation pathway of fluorine in the degradation of OFL by the Co-RM/PDS system, the concentration of F^- in the system before and after the reaction was determined using a fluorine ion-selective electrode to investigate the defluorination efficiency of Co-RM-Catalyst. Co-RM-activated PDS was used to degrade OFL at three different temperatures (20 °C, 30 °C, and 40 °C). The relationship between defluorination rate and reaction time at different temperatures is shown in Figure S6a. As the temperature increased, the removal effect of F^- in OFL was improved by the Co-RM/PDS system. The rate of defluorination in the Co-RM/PDS system showed a trend of rapidly increasing at first and then slowly increasing. The maximum defluorination rates of the reaction system at 20–40 °C were 40.32%, 50.34%, and 58.23%. At 30 min before the reaction, the rate of defluorination was linear with the reaction time, and the rate of

defluorination increased rapidly, indicating the adsorption of fluorine in OFL by the Co-RM/PDS system was an endothermic process. According to the Arrhenius equation [59], the rate constant k increases with increasing temperature. In turn, the positive reaction rate increases and the defluorination rate increases, which explains the increase of defluorination rate with increasing temperature. The defluorination rate showed a non-linear relationship with the reaction time within 30–90 min. The defluorination rate slowly changed to 60% with increasing reaction time, indicating the defluorination reaction of Co-RM-activated PDS started to be almost complete.

Formula (1) or Formula (2) is used to describe the relationship between defluorination rate φ and reaction time t, where the unit of t is min; k is the apparent rate constant, min^{-1}. The data in Figure S6a are transformed according to Equation (2), and linear fitting is performed. The fitting curve and fitting results are shown in Figure S6b and Table 3. The fitting results show the defluorination kinetic equation shown in formula (1) or (2) can better describe the relationship between defluorination rate φ and reaction time t.

$$\varphi = 12e^{-kt}, \tag{1}$$

$$\ln(1 - \varphi) = -kt. \tag{2}$$

Table 3. Fitting results of defluorination rate φ and reaction time t.

Kinetic Equation	Fitting Equation	Temperature (°C)	K (min^{-1})	R^2	r
		20	0.0060	0.9809	−0.9914
$\ln(1 - \varphi) = -kt$	y = a + bx	30	0.0079	0.9651	−0.9842
		40	0.0102	0.9182	−0.9625

4. Conclusions

In this paper, the effective activation of PDS by the Co-RM system for the oxidative degradation of OFL was demonstrated. PS was activated by the prepared modified RM catalyst to achieve the efficient removal of OFL. BET analysis showed the specific surface area of the catalyst increased and the pore volume decreased after calcination. SEM and EDS analysis showed Co was successfully loaded on RM. The removal rate of OFL increased with increasing PDS dose, Co-RM doses, and reaction temperature, which was inversely proportional to the initial concentration of OFL. The maximal removal rate of OFL by the Co-RM/PDS system was 80.06% under the following conditions: 15 mg/L OFL, 0.4 g/L Co-RM, 4 g/L PDS, 3.0 pH, and 40 °C temperature. In the Co-RM activation of PDS to decompose OFL, $SO_4^-\cdot$ was the main active substance in the reaction system, and HO· had an auxiliary removal effect. GC-MS analysis showed that during the degradation of OFL by defluorination, decarboxylation, piperazine, demethylation, ring opening, and other processes, smaller molecular weight intermediates such as m/z = 278, 149, 145 were received. These substances were further oxidized by active species and decomposed into small molecule substances and finally mineralized into inorganic small molecule substances such as H_2O, CO_2, and F^- to achieve the effective degradation of OFL. The established defluorination kinetic equation $\ln(1 - \varphi) = -kt$ can describe the relationship between defluorination rate and reaction time.

References

1. Hawash, H.B.; Moneer, A.A.; Galhoum, A.A.; Elgarahy, A.M.; Mohamed, W.A.A.; Samy, M.; El-Seedi, H.R.; Gaballah, M.S.; Mubarak, M.F.; Attia, N.F. Occurrence and spatial distribution of pharmaceuticals and personal care products (PPCPs) in the aquatic environment, their characteristics, and adopted legislations. *J. Water Process Eng.* **2023**, *52*, 103490. [CrossRef]

2. Wu, Y.; Xu, H.-Y.; Li, Z.-H.; Zhu, J.-Y.; Bai, J.-W.; Shao, Y.-F.; Lin, C.-C.; Guan, C.-Y. Magnetic pyro-hydrochar derived from waste cartons as an efficient activator of peroxymonosulfate for antibiotic dissipation. *Sep. Purif. Technol.* **2023**, *311*, 123288. [CrossRef]

3. Li, T.; Lu, S.; Lin, W.; Ren, H.; Zhou, R. Heat-activated persulfate oxidative degradation of ofloxacin: Kinetics, mechanisms, and toxicity assessment. *Chem. Eng. J.* **2022**, *433*, 133801. [CrossRef]

4. Wu, Y.; Zhu, J.-Y.; Bai, J.-W.; Lin, L.-F.; Yu, C.-P. The ability of pre-magnetized zero-valent iron for peroxymonosulfate activation to remove ofloxacin. *Chem. Eng. J.* **2023**, *461*, 141825. [CrossRef]

5. Maged, A.; Elgarahy, A.M.; Haneklaus, N.H.; Gupta, A.K.; Show, P.L.; Bhatnagar, A. Sustainable functionalized smectitic clay-based nano hydrated zirconium oxides for enhanced levofloxacin sorption from aqueous medium. *J. Hazard. Mater.* **2023**, *452*, 131325. [CrossRef]

6. Wang, J.; Zhuan, R. Degradation of antibiotics by advanced oxidation processes: An overview. *Sci. Total Environ.* **2020**, *701*, 135023. [CrossRef]

7. Wu, S.; Hu, H.; Lin, Y.; Zhang, J.; Hu, Y.H. Visible light photocatalytic degradation of tetracycline over TiO_2. *Chem. Eng. J.* **2020**, *382*, 122842. [CrossRef]

8. Li, Z.; Wang, J.; Chang, J.; Fu, B.; Wang, H. Insight into advanced oxidation processes for the degradation of fluoroquinolone antibiotics: Removal, mechanism, and influencing factors. *Sci. Total Environ.* **2023**, *857 Pt 2*, 159172. [CrossRef]

9. Sun, Y.; Li, D.; Zhou, S.; Shah, K.J.; Xiao, X. Research Progress of Advanced Oxidation. *Water Treat. Technol.* **2021**, *102*, 1–47.

10. Wang, L.; Yang, H.; Guo, M.; Wang, Z.; Zheng, X. Adsorption of antibiotics on different microplastics (MPs): Behavior and mechanism. *Sci. Total Environ.* **2023**, *863*, 161022. [CrossRef]

11. Wang, X.; Wang, B.; Chen, Y.; Wang, M.; Wu, Q.; Srinivas, K.; Yu, B.; Zhang, X.; Ma, F.; Zhang, W. Fe_2P nanoparticles embedded on Ni2P nanosheets as highly efficient and stable bifunctional electrocatalysts for water splitting. *J. Mater. Sci. Technol.* **2022**, *105*, 266–273. [CrossRef]

12. Mathur, P.; Sanyal, D.; Callahan, D.L.; Conlan, X.A.; Pfeffer, F.M. Treatment technologies to mitigate the harmful effects of recalcitrant fluoroquinolone antibiotics on the environment and human health. *Environ. Pollut.* **2021**, *291*, 118233. [CrossRef] [PubMed]

13. Nasrollahi, N.; Vatanpour, V.; Khataee, A. Removal of antibiotics from wastewaters by membrane technology: Limitations, successes, and future improvements. *Sci. Total Environ.* **2022**, *838 Pt 1*, 156010. [CrossRef] [PubMed]

14. He, Y.; Cai, Y.; Fan, S.; Meng, T.; Zhang, Y.; Li, X.; Zhang, Y. Hydroxyl radicals can significantly influence the toxicity of ofloxacin transformation products during ozonation. *J. Hazard. Mater.* **2022**, *438*, 129503. [CrossRef] [PubMed]

15. Li, S.; Wu, Y.; Zheng, H.; Li, H.; Zheng, Y.; Nan, J.; Ma, J.; Nagarajan, D.; Chang, J.S. Antibiotics degradation by advanced oxidation process (AOPs): Recent advances in ecotoxicity and antibiotic-resistance genes induction of degradation products. *Chemosphere* **2022**, *311 Pt 2*, 136977. [CrossRef]

16. Wang, H.; Mustafa, M.; Yu, G.; Ostman, M.; Cheng, Y.; Wang, Y.; Tysklind, M. Oxidation of emerging biocides and antibiotics in wastewater by ozonation and the electro-peroxone process. *Chemosphere* **2019**, *235*, 575–585. [CrossRef]

17. Zhang, X.-W.; Lan, M.-Y.; Wang, F.; Wang, C.-C.; Wang, P.; Ge, C.; Liu, W. Immobilized N-C/Co derived from ZIF-67 as PS-AOP catalyst for effective tetracycline matrix elimination: From batch to continuous process. *Chem. Eng. J.* **2022**, *450*, 138082. [CrossRef]

18. Ji, J.; Yuan, X.; Zhao, Y.; Jiang, L.; Wang, H. Mechanistic insights of removing pollutant in adsorption and advanced oxidation processes by sludge biochar. *J. Hazard. Mater.* **2022**, *430*, 128375. [CrossRef]

19. Li, Y.; Fan, J.; Feng, X.; Tao, T. Degradation of organics using LaFeO$_3$ as a persulfate activator under low-intensity ultra-violet-light irradiation: Catalytic performance and mechanism. *J. Rare Earths* **2022**, *40*, 1043–1052. [CrossRef]

20. Xu, Z.; Wu, Y.; Wang, X.; Ji, Q.; Li, T.; He, H.; Song, H.; Yang, S.; Li, S.; Yan, S.; et al. Identifying the role of oxygen vacancy on cobalt-based perovskites towards peroxymonosulfate activation for efficient iohexol degradation. *Appl. Catal. B Environ.* **2022**, *319*, 121901. [CrossRef]

21. Zhang, Y.; Zhou, J.; Chen, J.; Feng, X.; Cai, W. Rapid degradation of tetracycline hydrochloride by heterogeneous photocatalysis coupling persulfate oxidation with MIL-53(Fe) under visible light irradiation. *J. Hazard. Mater.* **2020**, *392*, 122315. [CrossRef] [PubMed]

22. Gu, J.; Wei, G.; Zhu, Y.; Lu, C.; Zhang, L.; Huang, Z.; Su, Q.; Pan, S. Photoelectric activation of persulfate with a new type of red mud-based CuFe$_2$O$_4$ particle electrode for the efficient degradation of ciprofloxacin: Preparation, influencing factors and mechanism. *J. Environ. Chem. Eng.* **2023**, *11*, 109137. [CrossRef]

23. Wang, L.; Luo, D.; Yang, J.; Wang, C. Metal-organic frameworks-derived catalysts for contaminant degradation in persulfate-based advanced oxidation processes. *J. Clean. Prod.* **2022**, *375*, 134118. [CrossRef]

24. Xiao, R.; Luo, Z.; Wei, Z.; Luo, S.; Spinney, R.; Yang, W.; Dionysiou, D.D. Activation of peroxymonosulfate/persulfate by nanomaterials for sulfate radical-based advanced oxidation technologies. *Curr. Opin. Chem. Eng.* **2018**, *19*, 51–58. [CrossRef]

25. Yoon, K.; Cho, D.-W.; Wang, H.; Song, H. Co-pyrolysis route of chlorella sp. and bauxite tailings to fabricate metal-biochar as persulfate activator. *Chem. Eng. J.* **2022**, *428*, 132578. [CrossRef]

26. Zhao, W.; Shen, Q.; Nan, T.; Zhou, M.; Xia, Y.; Hu, G.; Zheng, Q.; Wu, Y.; Bian, T.; Wei, T.; et al. Cobalt-based catalysts for heterogeneous peroxymonosulfate (PMS) activation in degradation of organic contaminants: Recent advances and perspectives. *J. Alloys Compd.* **2023**, *958*, 170370. [CrossRef]

27. Zhang, J.; Gao, Y.; Li, Z.; Wang, C. Pb^{2+} and Cr^{3+} immobilization efficiency and mechanism in red-mud-based geopolymer grouts. *Chemosphere* **2023**, *321*, 138129. [CrossRef]

28. Zakira, U.; Zheng, K.; Xie, N.; Birgisson, B. Development of high-strength geopolymers from red mud and blast furnace slag. *J. Clean. Prod.* **2023**, *383*, 135439. [CrossRef]

29. Chen, J.; Wang, Y.; Liu, Z. Red mud-based catalysts for the catalytic removal of typical air pollutants: A review. *J. Environ. Sci.* **2023**, *127*, 628–640. [CrossRef]

30. Liu, X.; Han, Y.; He, F.; Gao, P.; Yuan, S. Characteristic, hazard and iron recovery technology of red mud—A critical review. *J. Hazard. Mater.* **2021**, *420*, 126542. [CrossRef] [PubMed]

31. Su, Q.; Li, J.; Wang, B.; Li, Y. Direct Z-scheme Bi$_2$MoO$_6$/UiO-66-NH$_2$ heterojunctions for enhanced photocatalytic degradation of ofloxacin and ciprofloxacin under visible light. *Appl. Catal. B Environ.* **2022**, *318*, 121820. [CrossRef]

32. Li, Y.; Huang, H.; Xu, Z.; Ma, H.; Guo, Y. Mechanism study on manganese(II) removal from acid mine wastewater using red mud and its application to a lab-scale column. *J. Clean. Prod.* **2020**, *253*, 119955. [CrossRef]

33. Sing, K.S.W. Reporting physisorption data for gas/solid systems with special reference to the determination of surface area and porosity. *Pure Appl. Chem.* **1985**, *57*, 603–619. [CrossRef]

34. Song, L.; Nan, J.; Liu, B.; Wu, F. Novel three-dimensional Ti$_3$C$_2$-MXene embedded zirconium alginate aerogel adsorbent for efficient phosphate removal in water. *Chemosphere* **2023**, *319*, 138016. [CrossRef] [PubMed]

35. Sych, N.V.; Trofymenko, S.I.; Poddubnaya, O.I.; Tsyba, M.M.; Sapsay, V.I.; Klymchuk, D.O.; Puziy, A.M. Porous structure and surface chemistry of phosphoric acid activated carbon from corncob. *Appl. Surf. Sci.* **2012**, *261*, 75–82. [CrossRef]

36. Zhang, T.; Zhou, F.; Huang, J.; Man, R. Ethylene glycol dimethacrylate modified hyper-cross-linked resins: Porogen effect on pore structure and adsorption performance. *Chem. Eng. J.* **2018**, *339*, 278–287. [CrossRef]

37. Zhang, Y.; Jing, X.; Wang, Q.; Zheng, J.; Zhang, S.; Hu, T.; Meng, C. Hydrothermal synthesis and electrochemical properties of hierarchical vanadyl hydroxide spheres with hollow core and mesoporous shell. *Microporous Mesoporous Mater.* **2017**, *249*, 137–145. [CrossRef]

38. Huang, Y.; Zheng, H.; Hu, X.; Wu, Y.; Tang, X.; He, Q.; Peng, S. Enhanced selective adsorption of lead(II) from complex wastewater by DTPA functionalized chitosan-coated magnetic silica nanoparticles based on anion-synergism. *J. Hazard. Mater.* **2022**, *422*, 126856. [CrossRef] [PubMed]

39. Ioannidi, A.; Oulego, P.; Collado, S.; Petala, A.; Arniella, V.; Frontistis, Z.; Angelopoulos, G.N.; Diaz, M.; Mantzavinos, D. Persulfate activation by modified red mud for the oxidation of antibiotic sulfamethoxazole in water. *J. Environ. Manag.* **2020**, *270*, 110820. [CrossRef] [PubMed]

40. Jiang, H.; Zhu, C.; Yuan, Y.; Yue, C.; Ling, C.; Liu, F.; Li, A. Enhanced activation of peroxymonosulfate with metal-substituted hollow MxCo$_3$-xS$_4$ polyhedrons for superfast degradation of sulfamethazine. *Chem. Eng. J.* **2020**, *384*, 123302. [CrossRef]

41. Gokulakrishnan, S.; Parakh, P.; Prakash, H. Degradation of Malachite green by Potassium persulphate, its enhancement by 1,8-dimethyl-1,3,6,8,10,13-hexaazacyclotetradecane nickel(II) perchlorate complex, and removal of antibacterial activity. *J. Hazard. Mater.* **2012**, *213–214*, 19–27. [CrossRef] [PubMed]

42. Chen, G.; Wu, G.; Li, N.; Lu, X.; Zhao, J.; He, M.; Yan, B.; Zhang, H.; Duan, X.; Wang, S. Landfill leachate treatment by persulphate related advanced oxidation technologies. *J. Hazard. Mater.* **2021**, *418*, 126355. [CrossRef] [PubMed]

43. Wang, Z.; Fang, Y.; Yang, Y.; Qiu, B.; Li, H. Vacancies-rich MOFs-derived magnetic CoFe encapsulated in N-doped carbon nanotubes as peroxymonosulfate activator for p-arsanilic acid removal. *Chem. Eng. J.* **2023**, *454*, 140474. [CrossRef]

44. Gao, Y.; Zhao, Z.; Song, L.; Cao, D.; Zhou, S.; Gao, T.; Shang, J.; Cheng, X. Eggshell supported Cu doped FeOx magnetic nanoparticles as peroxymonosulfate activator for carbamazepine degradation. *Chem. Eng. J.* **2023**, *454*, 140282. [CrossRef]

45. Othman, I.; Hisham Zain, J.; Abu Haija, M.; Banat, F. Catalytic activation of peroxymonosulfate using $CeVO_4$ for phenol degradation: An insight into the reaction pathway. *Appl. Catal. B Environ.* **2020**, *266*, 118601. [CrossRef]

46. Sun, X.; He, K.; Chen, Z.; Yuan, H.; Guo, F.; Shi, W. Construction of visible-light-response photocatalysis-self-Fenton system for the efficient degradation of amoxicillin based on industrial waste red mud/CdS S-scheme heterojunction. *Sep. Purif. Technol.* **2023**, *324*, 124600. [CrossRef]

47. Liu, F.; Yi, P.; Wang, X.; Gao, H.; Zhang, H. Degradation of Acid Orange 7 by an ultrasound/ZnO-GAC/persulfate process. *Sep. Purif. Technol.* **2018**, *194*, 181–187. [CrossRef]

48. Wang, Y.; Huang, Y.; Gou, G.; Li, N.; Li, L.; He, Y.; Liu, C.; Lai, B.; Sun, H. Dispersed cobalt embedded nitrogen-rich carbon framework activates peroxymonosulfate for carbamazepine degradation: Cobalt leaching restriction and mechanism investigation. *Chemosphere* **2023**, *321*, 138026. [CrossRef]

49. Zhu, L.; Shen, D.; Zhang, H.; Luo, K.H.; Li, C. Fabrication of Z-scheme $Bi_7O_9I_3$/g-C_3N_4 heterojunction modified by carbon quantum dots for synchronous photocatalytic removal of Cr (VI) and organic pollutants. *J. Hazard. Mater.* **2023**, *446*, 130663. [CrossRef]

50. He, Y.; Qian, J.; Wang, P.; Wu, J.; Lu, B.; Tang, S.; Gao, P. Acceleration of levofloxacin degradation by combination of multiple free radicals via MoS_2 anchored in manganese ferrite doped perovskite activated PMS under visible light. *Chem. Eng. J.* **2022**, *431*, 133933. [CrossRef]

51. Cao, T.; Xu, J.; Chen, M. Construction of 2D/0D direct Z-scheme $Bi_4O_5I_2$/Bi_3TaO_7 heterojunction photocatalysts with enhanced activity for levofloxacin degradation under visible light irradiation. *Sep. Purif. Technol.* **2022**, *291*, 120896. [CrossRef]

52. Ma, Q.; Zhang, H.; Zhang, X.; Li, B.; Guo, R.; Cheng, Q.; Cheng, X. Synthesis of magnetic CuO/$MnFe_2O_4$ nanocompisite and its high activity for degradation of levofloxacin by activation of persulfate. *Chem. Eng. J.* **2019**, *360*, 848–860. [CrossRef]

53. Lei, J.; Chen, B.; Zhou, L.; Ding, N.; Cai, Z.; Wang, L.; In, S.-I.; Cui, C.; Zhou, Y.; Liu, Y.; et al. Efficient degradation of antibiotics in different water matrices through the photocatalysis of inverse opal K-g-C_3N_4: Insights into mechanism and assessment of antibacterial activity. *Chem. Eng. J.* **2020**, *400*, 125902. [CrossRef]

54. Gao, Y.; Zou, D. Efficient degradation of levofloxacin by a microwave–3D $ZnCo_2O_4$/activated persulfate process: Effects, degradation intermediates, and acute toxicity. *Chem. Eng. J.* **2020**, *393*, 124795. [CrossRef]

55. Zhou, J.; Liu, W.; Cai, W. The synergistic effect of Ag/AgCl@ZIF-8 modified g-C_3N_4 composite and peroxymonosulfate for the enhanced visible-light photocatalytic degradation of levofloxacin. *Sci. Total Environ.* **2019**, *696*, 133962. [CrossRef] [PubMed]

56. Li, S.; Wang, C.; Cai, M.; Yang, F.; Liu, Y.; Chen, J.; Zhang, P.; Li, X.; Chen, X. Facile fabrication of TaON/Bi_2MoO_6 core–shell S-scheme heterojunction nanofibers for boosting visible-light catalytic levofloxacin degradation and Cr(VI) reduction. *Chem. Eng. J.* **2022**, *428*, 131158. [CrossRef]

57. Sun, H.; Qin, P.; Wu, Z.; Liao, C.; Guo, J.; Luo, S.; Chai, Y. Visible light-driven photocatalytic degradation of organic pollutants by a novel Ag_3VO_4/Ag_2CO_3 p–n heterojunction photocatalyst: Mechanistic insight and degradation pathways. *J. Alloys Compd.* **2020**, *834*, 155211. [CrossRef]

58. Pang, Y.; Zhou, J.; Yang, X.; Lan, Y.; Chen, C. Rationally designed Co_3O_4-SnO_2 activated peroxymonosulfate for the elimination of chloramphenicol. *Chem. Eng. J.* **2021**, *418*, 129401. [CrossRef]

59. Youssef, A.A.A.; Salas, A.H.; Al-Harbi, N.; Basfer, N.M.; Nassr, D.I. Determination of chemical kinetic parameters in Arrhenius equation of constant heating rate: Theoretical method. *Alex. Eng. J.* **2023**, *67*, 461–472. [CrossRef]